Structure and dynamics of a self-propelled semiflexible filament

Shalabh K. Anand* and Sunil P. Singh†
Department of Physics, Indian Institute of Science Education and Research, Bhopal 462 066, Madhya Pradesh, India

(Received 14 July 2018; published 3 October 2018)

We investigate structural and dynamical properties of a self-propelled filament using coarse-grained Brownian dynamics simulations. A self-propulsion force is applied along the bond vectors, i.e., tangent to the filament and their locations are considered in two different manners. In case one, force is applied to all beads of the filament, which is termed as homogeneous self-propulsion. Here we obtain a monotonic decrease in the stiffness of the filament with Péclet number, hence, radius of gyration also displays the same trend. Moreover, the radius of gyration of the filament shows universal dependence for various bending rigidities with flexure number. The effective diffusivity of the filament shows enhancement with the active force, and it increases linearly with force, and bending rigidity. In case two, self-propulsion force is applied only to a few bond vectors. The location of active forces is chosen in a periodic manner starting from the tail of the filament and leaving the front end without force. In this case, the filament acquires various structures such as the rodlike, helical, circular, and folded states. The transition from several states is understood in terms of tangent-tangent correlation, bending energy, and torsional order parameter. The helical state is identified through a crossover from exponential to oscillatory behavior of the tangent-tangent correlation. A sudden increase in the bending energy separates a helical state to a folded state of the filament.

DOI: 10.1103/PhysRevE.98.042501

I. INTRODUCTION

Study of active matter systems such as a flock of birds [1], a school of fishes [2], bacterial colonies [3], motility of spermatozoa, etc., has drawn immense research interest in recent years [4–6]. Their movement is fuelled by chemical energy, which is converted into mechanical energy. The presence of local excess energy drives the system out of equilibrium. Understanding behavior of driven systems is an intense area of research from the fundamental aspect. One of the widely studied systems is the active filament, which is regarded as thin and long polymer chains [7–16]. Several types of active filaments are found in the cell, and they play a decisive role in providing shape, structure, and motility to cell membranes [17]. Moreover, many microswimmers propel themselves by long hairy polymeric structures, such as cilia and flagella [5,18,19]. These active filaments exhibit fascinating structural, dynamical, and collective behaviors [20–26].

In the recent past, various studies have been done on active filaments using theoretical [7–9] and simulation models [7,13–15]. In these models, either self-propulsion force is imposed tangential to the filament [7,13–15,27] or monomers of the filament are treated as active Brownian particles [8,9,11]. A freely moving active filament acquires numerous dynamical conformations, such as rotational motion, snakelike motion [13,14], straight translational motion [10,16], etc. The rigidity of a filament plays a crucial role in its conformational behavior, as a flexible polymer swells under strong active force [11], while a semiflexible filament shrinks under activity. However, in an extreme propulsion limit, the polymer swells again [8,9]. A clamped filament shows beating and spontaneous rotational motion under tangential compressive force [15,27]. Presence of a load in front shows a stable circular, beating, and spiral structures on the surfaces in the absence of hydrodynamics [13,14]. However, hydrodynamic interactions induce instability to a filament when actuated with an active colloid on its terminus [15].

Internal relaxation of a filament is altered in the presence of active force. The change in relaxation time is determined by the strength of force and their correlations [28]. The longest relaxation time shows a crossover from a bending dominated limit to a flexible limit under strong active force [8,9]. Active medium and the strength of the force influences the diffusive behavior of the filament. Interestingly, an active filament shows enhanced diffusion as well as superdiffusive behavior. In a viscoelastic medium with active bath [29,30], mean-square displacement of the center-of-mass of filament, as well as monomers display superdiffusive behavior [7,29,30]. This dynamical aspect of the filament has been reported in several experimental investigations in cellular medium, cytoskeletons, and chromatins [31–35].

In this article, we investigate a freely moving self-propelled filament in bulk (three dimensions) using overdamped Langevin dynamics. The self-propulsion force is imposed tangentially to the filament. Two different cases are considered for the tangential self-propulsion. In the case one, active force is applied homogeneously along the filament on each bond [Fig. 1(a)]. In the second case, the role of inhomogeneity is considered in an averaged manner. Thus the self-propulsion force is applied only to a few bonds on the filament, and their location is chosen in a periodic manner as shown in Fig. 1(b). This can be understood as follows:

*skanand@iiserb.ac.in
†spsingh@iiserb.ac.in

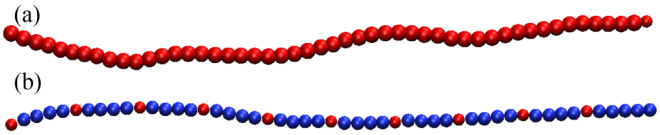

FIG. 1. Figure displays arrangement of the active monomers on the filament in red and passive monomers are in blue. Top filament (a) corresponds for the homogeneous self-propulsion and the bottom one (b) is for the periodic sequence of the active monomers. Distance between two successive monomers is $l_a = 5$ (in simulation units).

A filament is divided into equal length of segments, and active force is placed on the tail of each segment as shown in Fig. 1(b) in red. In this case, front monomers are passive, which acts as a load. So far the role of periodic sequence of self-propulsion on a filament has not been investigated in detail. In our simulations, hydrodynamic interactions are ignored for the simplicity of the calculation.

A freely swimming self-propelled filament buckles under the compressive force. We obtain that the structural change, under homogeneous self-propulsion, shows a universal behavior for various bending rigidities with respect to a dimensionless parameter called flexure number. In the periodic self-propulsion, a filament undergoes transition from the extended state to a circular, helical, and folded or strongly buckled states. Our main emphasis in this article is to identify several phases emerging under various self-propulsion arrangements. To do so, we have calculated torsional order parameter [12], bending energy, and tangent-tangent correlation of the filament [36]. In the extended state, the torsional parameter is small and becomes very large in helical and folded states. Furthermore, structural correlations along the filament exhibit oscillatory behavior, and the curvature radius of the helical phase shows a power-law variation with force.

The article is organized as follows. In Sec. II, we discuss a coarse-grained model for the self-propelled filament. Structural and dynamical behavior of the homogeneously self-propelled filament is presented in Sec. III. Results for the periodically arranged self-propelled monomers on the filament are discussed in Sec. IV. A summary of the results is presented in Sec. V.

II. SIMULATION MODEL

We model filament as a semiflexible linear polymer composed of a sequence of N monomeric units connected via Harmonic spring. All the monomers in the polymer also interact via excluded volume interactions. The total potential energy of the filament can be written as $U = U_h + U_b + U_{\rm LJ}$, where U_h is spring potential, U_b is bending potential, and $U_{\rm LJ}$ corresponds to excluded volume potential (Lennard-Jones). Harmonic potential is given as

$$U_h = \frac{k_s}{2}\sum_{i=1}^{N-1}(|\boldsymbol{r}_{i+1} - \boldsymbol{r}_i| - l_0)^2, \tag{1}$$

where l_0 is the average equilibrium bond length, $\mathbf{r}_i$ is position vector of the ith monomer, and k_s is the spring constant. Bending potential energy U_b, which accounts for the stiffness of the polymer, is written as

$$U_b = \frac{\kappa}{2}\sum_{i=1}^{N-2}(\boldsymbol{R}_{i+1} - \boldsymbol{R}_i)^2, \tag{2}$$

here R_i is length of the ith bond vector, defined as $\mathbf{R}_i = \mathbf{r}_{i+1} - \mathbf{r}_i$, and κ is the bending rigidity of the polymer which can be expressed in terms of persistence length of the polymer l_p as, $l_p = \kappa l_0^3/k_BT$, where k_BT is thermal energy.

Excluded volume potential avoids overlap of beads in a polymer, and its form is taken from the truncated repulsive part of the Lennard-Jones potential, i.e., $R_{ij} < 2^{1/6}\sigma$,

$$U_{\rm LJ} = \sum_{i=1}^{N-1}\sum_{j=i+1}^{N} 4\epsilon\left[\left(\frac{\sigma}{R_{ij}}\right)^{12} - \left(\frac{\sigma}{R_{ij}}\right)^{6} + \frac{1}{4}\right], \tag{3}$$

and for $R_{ij} \geqslant 2^{1/6}\sigma$, it is considered as $U_{\rm LJ} = 0$. Here ϵ is the LJ interaction energy and σ is the LJ diameter of the monomer.

Newton's equation of motion for a monomer in overdamped limit is

$$\gamma\frac{d\boldsymbol{r}_i}{dt} = -\nabla_i U + \mathbf{F}_r^i + \mathbf{F}_a^i, \tag{4}$$

where γ is the friction coefficient, $\mathbf{F}_r^i$ is the thermal noise with zero mean, and $\mathbf{F}_a^i$ is the self-propulsion force which is exerted on the ith bond vector. Since hydrodynamics interactions are ignored in the simulations thereby solvent-mediated indirect coupling among the monomers is absent in the equation of motion.

The viscous drag and the thermal noise are related through the fluctuation-dissipation relation

$$\left\langle \mathbf{F}_r^i(t)\cdot\mathbf{F}_r^j(t')\right\rangle = 6k_BT\gamma\delta_{ij}\delta(t-t'). \tag{5}$$

Total self-propulsion force on the polymer is given as

$$\mathbf{F}_a^T = \sum_{i=1}^{N}\mathbf{F}_a^i = \sum_{i=1}^{N-1} f_a\mathbf{t}(\mathbf{r}_i)\Theta(r_i), \tag{6}$$

where $\mathbf{t}(\mathbf{r}_i) = (\boldsymbol{r}_{i+1} - \boldsymbol{r}_i)/|\boldsymbol{r}_{i+1} - \boldsymbol{r}_i|$ is unit tangent vector on the ith monomer. Active force is shared equally between ith and $(i+1)$th monomers as $f_a/2$. If the step function $\Theta(r_i) = 1$, then the ith monomer is active. Similarly, if $\Theta(r_i) = 0$, then the monomer will be passive. We consider here two different arrangements of self-propulsion force on the filament described as follows. (i) Homogenous self-propulsion: Active force is applied on each bond of the polymer, therefore all monomers feel active force. We term it *homogenous self-propulsion*. (ii) Periodic sequence of self-propulsion: In this case, propulsion force is applied to a few bonds arranged in a periodic sequence. Placement of active monomers starts from the tail of filament in an equidistant manner with leaving front end as passive. Figure 1(b) displays the clear picture of the periodic arrangement of active monomers on the filament.

In the periodic self-propulsion, the number of active monomers are taken as a variable parameter which varies from $N_a = 0$ to $N_a = N$. Here, $N_a = 0$ corresponds to the passive filament, while $N_a = N$ recovers the homogeneous self-propulsion. The strength of the active force is defined in

units of thermal energy called as Péclet number, which is a dimensionless number. It is defined here as $\mathrm{Pe} = \frac{f_a l_0}{k_B T}$. In the limit of $\mathrm{Pe} << 1$, thermal fluctuations dominate. However, in the limit of $\mathrm{Pe} >> 1$, active force dominates. The ratio of the Péclet number (Pe) and the scaled persistence length (l_p/l_0) is a dimensionless parameter given as $\chi = l_0 \mathrm{Pe}/l_p$. Here χ is called flexure number, which provides a measure of active force over the bending rigidity. Flexure number is used to understand the buckling instabilities [27,37], spontaneous spiral formation, spiral stability, and rotational motion [13,14] of active filaments.

All the physical parameters presented here are scaled in units of the bond length l_0, diffusion coefficient of a monomer D_m, and thermal energy $k_B T$. Simulations parameters are chosen as $k_s = 1000 k_B T/l_0^2$, $\sigma = l_0$, $\epsilon/k_B T = 1$, time is in units of $\tau = l_0^2/D_m$, and the stiffness parameter κ is in units of $k_B T/l_0^2$. The separation between two consecutive active sites is considered in the range of $l_a = 1$ ($N_a = 101$) to $l_a = 25$ ($N_a = 4$) and the bending rigidity of the polymer is varied in the range of $\kappa = 0$ to 200 for homogeneous self-propulsion, whereas for the patterned case we take $\kappa = 100$ and $\kappa = 40$. Unless explicitly mentioned, number of monomers in the chain is taken to be $N = 101$. We use the Euler integration technique to solve Eq. (4). The integration time step Δt is varied from the range of $10^{-2}\tau$ to $10^{-5}\tau$ to ensure stable simulation results. All the simulations are performed in a cubic periodic box.

A larger active force causes an increase in the average bond length, and thus it requires a larger spring constant. In addition to that, a smaller integration time step needs to be taken into account for better numerical accuracy. Thus, all simulations are restricted in the range of Péclet number 0 to 600. In order to ensure better statistics, each data point is averaged over 50 independent runs in a small Péclet number limit, i.e., $\mathrm{Pe} < 1$. However, the rest of the data points are averaged over 32 independent runs.

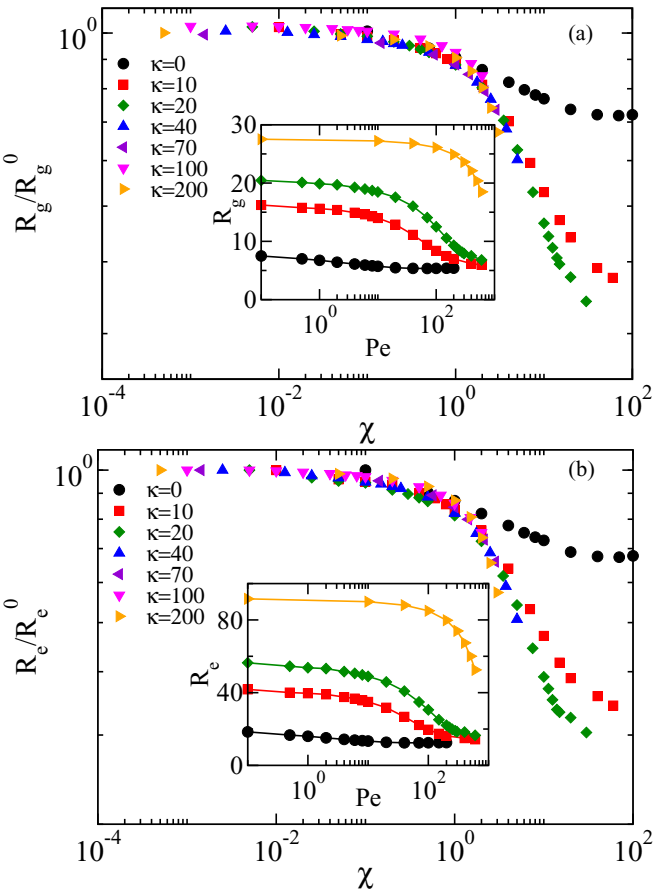

FIG. 2. Figure shows the relative change in the mean radius of gyration R_g/R_g^0 (a) and the end-to-end distance R_e/R_e^0 (b) with respect to its equilibrium values R_g^0 and R_e^0, respectively, as a function of flexure number χ. Inset of (a) and (b) shows the mean radius of gyration and the mean end-to-end distance R_e as a function of Pe. Various curves in (a) and (b) correspond to κ as displayed in the figures.

III. HOMOGENEOUS SELF-PROPULSION

In this section, we present results for homogeneous self-propulsion where all monomers are active. In equilibrium, structural and dynamical behaviors of the filament have been very well understood [38–43]. The presence of propulsion on the filament causes bending, and therefore its structural and dynamical behavior deviates from the equilibrium.

A. Structural properties

The structural change is analyzed by estimating average radius of gyration R_g and average end-to-end distance R_e of the filament. The radius of gyration and the end-to-end distance is computed by the expression

$$R_g^2 = \frac{1}{N}\left\langle \sum_{i=1}^{N} (\boldsymbol{r}_i - \boldsymbol{r}_{\mathrm{cm}})^2 \right\rangle;\ R_e^2 = \langle (\boldsymbol{r}_1 - \boldsymbol{r}_N)^2 \rangle, \qquad (7)$$

where $\boldsymbol{r}_{\mathrm{cm}}$ is the center-of-mass of the filament and angular brackets indicate the ensemble average of the physical quantities. Figure 2 shows the dependence of the radius of gyration and end-to-end distance on flexure number for various bending rigidities.

First, we discuss results of the flexible polymer, i.e., for $\kappa = 0$. In the weak active force, i.e., $\chi << 1$, the normalized radius of gyration R_g/R_g^0 decreases monotonically with increasing χ. Further increase in χ results in a relatively large change in R_g/R_g^0 and, eventually, in the limit of large $\chi > 10$, R_g is almost independent of χ, which is consistent with other simulations and theoretical results [8,9]. The saturation in R_g and R_e occurs due to excluded volume interactions which prevent collapse of a polymer.

Now we present results for the semiflexible filament. Here, the radius of gyration decreases with activity as displayed in Fig. 2. In the limit of weak active force, i.e., $\chi < 1$, the radius of gyration gradually decreases with χ similar to the flexible polymer. Further increase in active force, i.e., $\chi \geqslant 1$, the relative change in the radius of gyration increases substantially. Interestingly, for $\kappa > 10$, all the curves display nearly a universal behavior up to four orders of magnitude in χ as shown in Fig. 2. The end-to-end distance also reflects the same universal trend whose properties can be understood in terms of a single master curve in the limit of $\chi < 10$. In the semiflexible regime, R_g and R_e decreases monotonically with

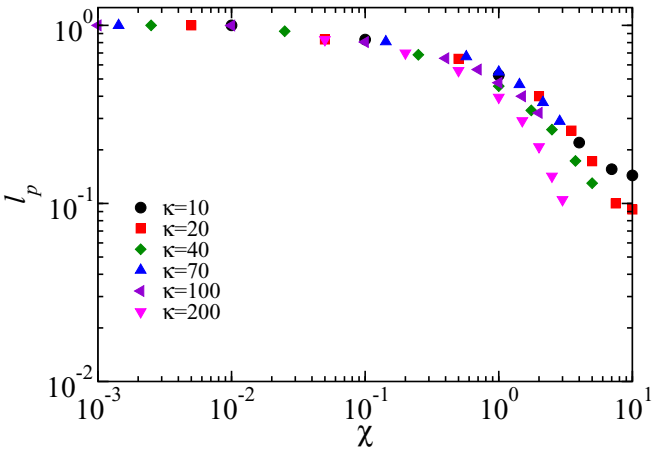

FIG. 3. The persistence length l_p as a function of χ for various $\kappa = 10, 20, 40, 70, 100$, and 200 for the polymer length $N = 101$.

χ. For $\chi \gg 1$, R_g approaches to a plateau value for $\kappa = 10$ and 20 similar to the flexible polymer limit as reflected in Figs. 2(a) and 2(b). The inset of Figs. 2(a) and 2(b) display absolute values of R_g and R_e as a function of Pe for various κ. This reflects the monotonic decrease of R_g and R_e in the range of Pe $\leqslant 10^2$. For the $\kappa \leqslant 20$, R_g and R_e are slowly approaching to a saturation limit. Note that for $\kappa > 20$, the saturation limit is not reached in displayed simulation range, which will appear in the limit of Pe $> 10^3$.

A filament shrinks under homogenous self-propulsion due to several competitive forces on it, which can be understood in terms of fluctuations in bond orientations due to the random motion of monomers. A bead always goes to random motion, which causes fluctuations in bond orientations along the contour. Hence tangential force pushes the filament along the randomly fluctuating bond directions, which leads to an increase in the average noise over the filament. Thus it bends and buckles with Pe, which results in the shrinkage of the filament. Considerably larger values of κ suppress bond fluctuations, and thus shrinkage of the polymer is smaller, even for the substantially large Péclet numbers.

The shrinkage in the radius of gyration with activity reflects a decrease in the rigidity of the polymer. To quantify the change in the rigidity, we compute its persistence length with active force. This can be computed from the tangent-tangent autocorrelation of the filament, which is expressed as $C(s) = \langle \mathbf{t}(\boldsymbol{r}_i) \cdot \mathbf{t}(\boldsymbol{r}_1) \rangle$, where s is the arc length and $s = |r_i - r_1| \equiv |i - 1|$. We have estimated correlation from one end of the polymer, i.e., from the tail for $i = 1, 2, \ldots, N - 1$. The correlation decays exponentially as $C(s) \sim \exp(-\frac{s}{l_p})$, with the arc length of the polymer for all values of Pe and κ. We calculate persistence length by fitting exponential function in the correlation function. Figure 3 displays the persistence length as a function of χ; as expected, l_p decreases monotonically for all κ in the limit of $\chi \leqslant 1$. In the limit of $\chi > 1$, active polymer becomes flexible, thereby persistence length $l_p \approx l_0$, and thus in the activity dominated regime $\chi > 1$, l_p nearly saturates as displayed in Fig. 3 for smaller $\kappa = 10$ and 20. In the limit of $\chi \leqslant 1$, all the curves display a universal behavior with κ as illustrated in the plot. The analysis of the persistence length suggests that a semiflexible polymer behave as a flexible polymer in the limit of large $\chi > 10$.

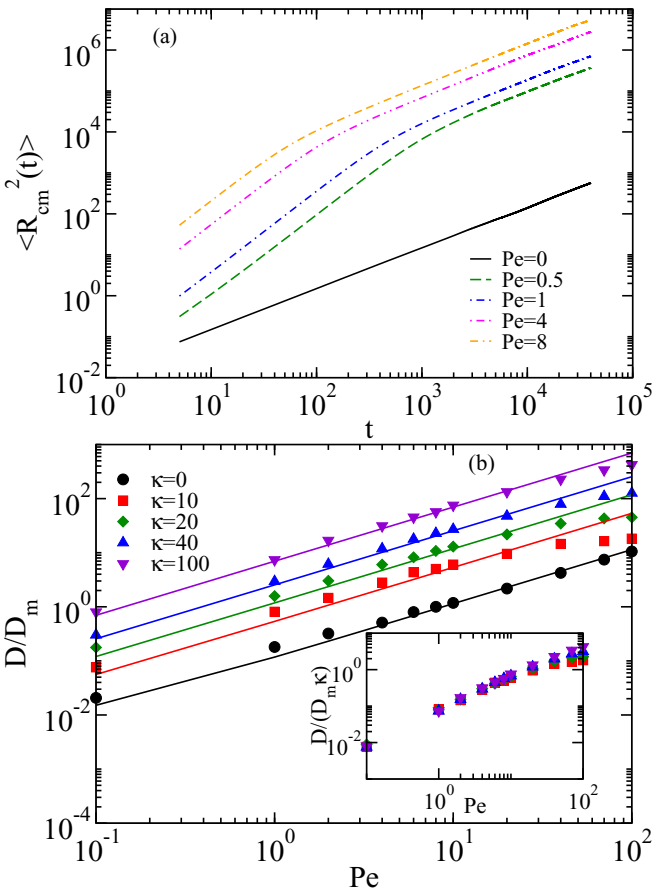

FIG. 4. (a) The mean-square displacement of the center-of-mass of the filament for $\kappa = 40$ for various Pe $= 0.0, 0.5, 1, 4$, and 8. (b) The scaled effective diffusivity D/D_m of the filament as a function Pe for various $\kappa = 0, 10, 20, 40$, and 100. Inset shows scaled diffusivity $D/(D_m\kappa)$ with Pe for $\kappa = 10, 20, 40$, and 100.

B. Diffusion of filament

In this section, we discuss dynamics of a filament under homogeneous self-propulsion by estimating mean-square displacement (MSD) of the center-of-mass. The MSD of a filament is computed as $\langle R_{\rm cm}^2(t) \rangle = \langle [r_{\rm cm}(t) - r_{\rm cm}(0)]^2 \rangle$, where angular brackets denote ensemble average. In equilibrium, qualitative behavior of the MSD of a filament can be separated into mainly two time regimes. The short-time limit is called the ballistic regime, where $\langle R_{\rm cm}^2(t) \rangle \sim t^2$; however, the long-time limit is called the diffusive regime, and here the MSD varies linearly in time as $\langle R_{\rm cm}^2(t) \rangle = 6Dt$, where D is the diffusion coefficient of the filament. Figure 4 displays the MSD of the filament with time for different Pe. The MSD of the passive filament is shown by the solid line. As expected, it reflects diffusive behavior in the long-time limit.

In the presence of tangential active force, the polymer is compressed and drifted along the end-to-end vector. Drift motion reflects the enhanced mean-square displacement of the center-of-mass in the intermediate time regime. Increase in the MSD is observed with Pe in all time regimes. It is evident from

the plot that the MSD exhibits superdiffusive behavior, i.e., $\langle R_{\rm cm}^2 \rangle \sim t^{\alpha}$, with exponent $\alpha > 1$, in the intermediate time regime. Further in the long-time limit, the MSD recovers the linear behavior. Another interesting observation is the shift in timescale of a superdiffusive regime to smaller time with Péclet number. This can be interpreted in terms of the flexibility and memory of directed motion. A filament becomes flexible with active force as shown in the structural analysis, which results in a decrease in the persistence length of the directed motion. Thereby, superdiffusive behavior persists relatively at smaller times. In a more intuitive way, we can also derive an approximate expression for the crossover time by equating the MSD expression in the ballistic regime, $\langle R_{\rm cm}^2(t_c) \rangle \sim (f_a t_c/\gamma)^2$, and diffusive regime, $\langle R_{\rm cm}^2(t_c) \rangle \sim D t_c$, which gives $t_c \sim D\gamma^2/f_a^2$.

The long-time diffusivity of the filament is obtained by fitting a linear function to the MSD curves. Figure 4(b) displays diffusivity of the polymer with Pe for several values of the rigidities. The diffusivity enhances with the Péclet number. Moreover, it increases linearly with Pe, as $D \sim g(\kappa)$Pe, where $g(\kappa)$ shows bending dependence of D for all κ as illustrated in Fig. 4. The effective diffusivity of the filament increases due to active fluctuations in the system. In an active medium, a modified form of the fluctuation-dissipation relation (FDR) is proposed that relates the measured effective diffusivity of a tracer particle with effective temperature as $D = k_B T_{\rm eff}/\gamma$ [44,45]. We use this relation to define the effective temperature $T_{\rm eff}$ in terms of long-time diffusivity of the filament. Thus the effective temperature of the filament increases with active force as also reported in Ref. [7].

The crossover time t_c defined above can be reexpressed in terms of Pe and effective diffusivity as $t_c \sim D/\text{Pe}^2$, and linear dependence of D on Pe gives $t_c \sim g(\kappa)/\text{Pe}$. The inset of Fig. 4(b) shows that $D/(\kappa D_m) \sim$ Pe, i.e., $g(\kappa) \sim \kappa$. Hence, we obtain, $t_c \sim \chi^{-1}$. Thus the crossover time decreases with increasing χ, and our simulations also show decreases in t_c with χ^{-1}.

The linear form of the diffusivity of a filament with Pe near the surfaces is also reported in previous studies [13,14]. At large bending parameters, persistence length of the directional motion increases therefore the diffusivity also increases, which shows linear increase as expected with κ for a given Péclet number. Thus, a stiffer filament diffuses relatively faster than the flexible polymer under homogeneous self-propulsion.

IV. PERIODIC SEQUENCE OF ACTIVE FORCE

In this section, we explore various conformations of the filament under equally spaced active monomers. Leaving front monomers as passive, which acts as a load, leads to bending of the filament under compression. The presence of activity on the front monomers pulls the front beads, which suppresses the buckling between the front active monomers. In addition, it also drags the filament along the same direction that leads to translation motion. Thereby, front monomers are always left as passive. Importance of load is discussed and analyzed in Sec. V for the case of inhomogeneous self-propulsion.

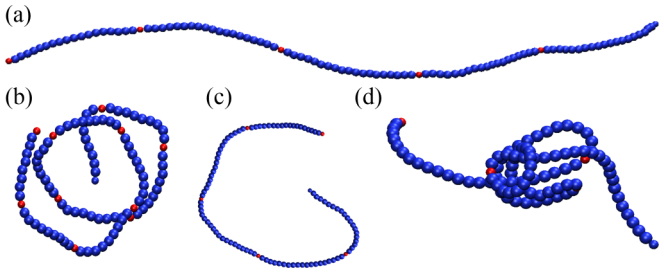

FIG. 5. Few snapshots of the filament showing different structures under periodic arrangement of active monomers. Red corresponds to the active monomer and blue represents the passive one. Top row represents the extended state (a). In the bottom row, helical (b), circular (c), and folded structures (d) are shown from left to right, respectively. The conformations of the filament are also shown in the attached movies [46].

The arrangement of the active force on the filament is shown in Fig. 1 for the separation $l_a = 5$. Here l_a is the distance between two successive active monomers. Interestingly, under a periodic sequence of the active force, a filament assumes interesting conformations during motion which is not observed in homogenous self-propulsion in bulk. These conformations depend on the spacing between active forces l_a, the strength of the propulsion, and the rigidity of the filament.

In small Péclet numbers, Pe < 1, a filament translates along the direction of the end-to-end vector, and thus its structure is weakly perturbed. In the intermediate regime of compressive force, the external force becomes comparable to the elastic energy. Therefore an active monomer pushes against passive monomers, which causes bending of the filament. Further increase in the force buckles the filament in a correlated manner throughout the filament. This occurs for the separation of the active monomers $l_a \geqslant 5$. In the case of correlated buckling, it forms a circular or helical structure. A circular phase appears in the range of $l_a \geqslant 14$ and in a narrow range of Pe. In our analysis, a circular phase is treated as a helical phase. This can be visualized as a helix of one turn with a very small pitch length. Further increase in the force pushes a filament strongly against the viscous drag, which causes uncorrelated buckling and it leads to distortion in the structure. Large forces result in sharp bending and twisting of the filament nearby the active monomers, and such sharply bent structures are called *folded structures* here.

Few snapshots of the filament in the extended, helical, circular, and folded states are shown in Fig. 5. We also show these structures in Supplementary Movies [46]. Our focus in this section is to identify helical, circular, and folded states of a self-propelled filament in the parameter space of Pe and l_a. To do so, we compute two-point tangent-tangent correlation of the bond vectors, the bending energy, and the torsional order parameter of the filament.

A. Helical phase

A helical phase can be distinguished using tangent-tangent correlation of the filament. The characteristic behavior of the helical state is function of l_a and Pe. To quantify the helical

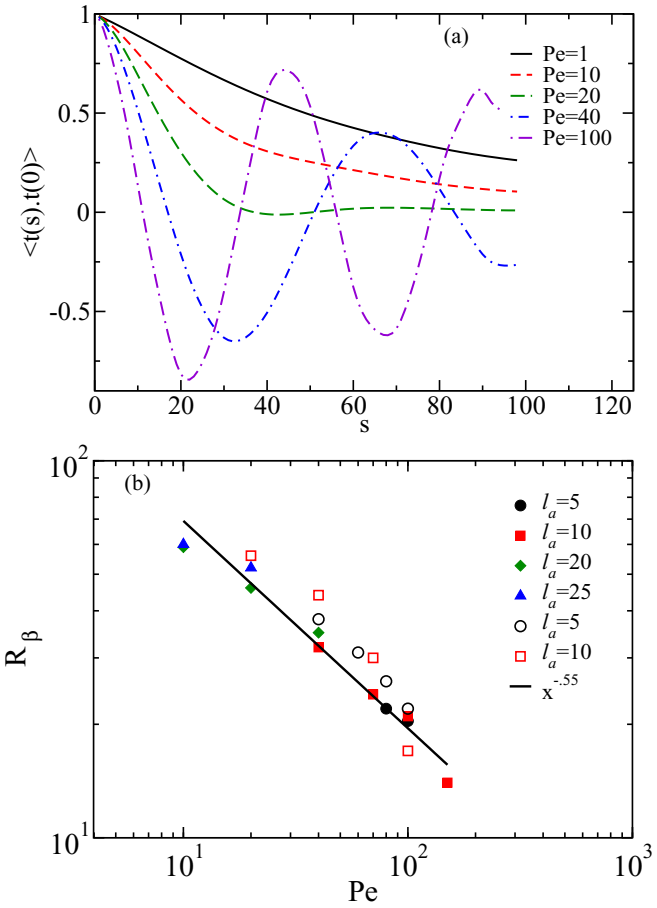

FIG. 6. (a) Figure displays tangent-tangent correlation function $\langle \mathbf{t}(s) \cdot \mathbf{t}(0) \rangle$ of the self-propelled filament at $l_a = 10$ and bending rigidity $\kappa = 100$. (b) Curvature radius R_β of the helical phase obtained from fitting Eq. (8) for various $l_a = 5, 10, 20$, and 25 for $\kappa = 100$ (filled symbols). Open symbols correspond to $l_a = 5$ and 10 at $\kappa = 40$. The solid line shows power behavior $(\mathrm{Pe})^{-.55}$ of the curvature radius.

state in the above parameter space, we compute tangent-tangent correlation functions of the filament as discussed earlier. Figure 6 shows variation of the correlation for a few Péclet numbers at $l_a = 10$. Here the correlation is computed from the end monomers as a function of arc length. The correlation function $C(s)$ decays exponentially in the weak force limit with s. For larger force, i.e., $\mathrm{Pe} = 20$, the correlation sharply reaches negative values and after approaching a minimum it tends to zero from the negative side. Further increase in Pe shows oscillations in the correlation. At larger Pe, these oscillations show long-range correlation. Strong correlation and sinusoidal behavior signify the underlying helical phase of the filament [36]. Note that, under homogenous self-propulsion, oscillatory behavior in the correlation is absent throughout the parameter regime presented in this article. Hence, we conclude that no helical structure occurs in this case. Therefore, crossover from the exponential to sinusoidal correlation is the signature of a helical phase. Sinusoidal behavior of correlation occurs in both circular and helical phases.

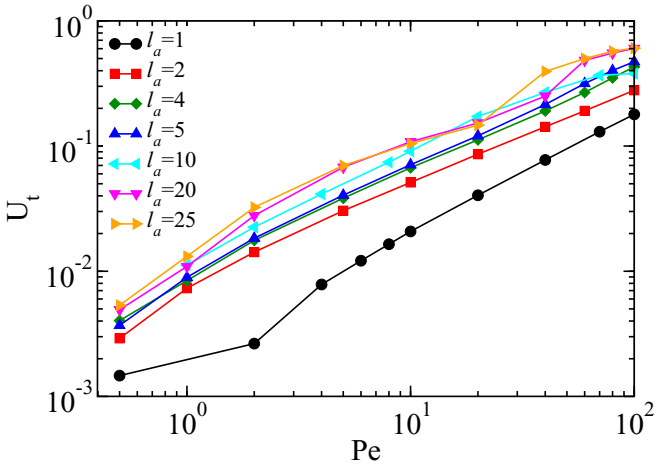

FIG. 7. Average torsional order parameter U_t as a function of Pe for various l_a as shown in the figure for a given $\kappa = 100$.

A characteristic length scale and wave number associated with the correlation can be estimated from the following expression:

$$C(s) = a_\beta \exp(-s/l_p)[\cos(2\pi s/R_\beta)], \tag{8}$$

where a_β is some constant and R_β is the length scale associated with the curvature radius of the filament. This function exhibits the property that it decays exponentially and captures oscillatory behavior as well. Fitting Eq. (8) in the tangent-tangent correlation gives the curvature of the filament, which is plotted in Fig. 6 as a function of Pe. As expected, curvature radius decreases with increasing compressive force. Interestingly, R_β for all the l_a's shows a similar trend and it follows a master curve without any scaling parameter as shown in the graph. Moreover, the master curve exhibits a power-law behavior with Péclet number, as $R_\beta \sim \mathrm{Pe}^{-\beta}$, with the exponent $\beta \sim 0.55$. The solid line in Fig. 6 is shown for visualisation of the power-law behavior with the same exponent. The curvature radius of the filament obtained here has slightly larger exponent compared to a buckled filament near the surfaces [12], which we believe is due to larger contour fluctuations in the bulk relative to the surfaces.

To show out-of-plane motion and twist of the filament in the helical phase, we compute average torsional order parameter of the filament. This is computed in a manner similar to that discussed in Ref. [12],

$$U_t = \sum_{i=2}^{N-1} \frac{1}{N-3} \cos\theta_i, \tag{9}$$

$$\cos\theta_i = \frac{(\vec{R}_{i-1} \times \vec{R}_i) \cdot (\vec{R}_i \times \vec{R}_{i+1})}{|\vec{R}_{i-1} \times \vec{R}_i||\vec{R}_i \times \vec{R}_{i+1}|},$$

where U_t is average of the sum of cosines of the torsion angle over the filament and θ_i is the angle given by three consecutive bond vectors $\vec{R}_{i-1}$, $\vec{R}_i$, and $\vec{R}_{i+1}$. Figure 7 displays U_t with Péclet number for various l_a. The torsional order parameter smoothly increases with Pe. Figure 7 displays U_t that is very small in the limit of $\mathrm{Pe} << 1$, further increase in Pe leads to a monotonic increase in the torsional order parameter. In

the limit of large Pe, U_t has increased nearly two orders of magnitude. Large values of U_t signifies that filament can be strongly twisted or folded, but it is not sufficient enough to delineate the helical structure. The combination of torsional order parameter and tangent-tangent correlation can precisely define the helical state. It would be important to mention here that torsional angle does not reflect any sharp transition from extended to helical and latter state to folded state. Rather, it varies smoothly from one phase to another phase with force [47].

Another interesting observation worth mentioning here is the increase in the torsional parameter with l_a for a given Pe. Fewer active monomers produce large amount of twist or out-of-plane motion to the filament. In the limit of small separations, translation motion is dominant and thus the change in torsional parameter is small. Increasing separations cause a larger drag force on the active monomers and thus it reduces the translation motion, which leads to buckling of the filament between active locations. This is reflected in the increase in torsion order parameter, and from this we infer that in order to have a correlated buckling large separation among the active monomers is essential.

B. Folded state

In this section, we quantify uncorrelated buckling of the filament. In the limit of large force, helical or circular states are followed by the folded state. In this structure, a filament is strongly folded near the active monomers due to large buckling. To distinguish the helical state from the folded state, we compute the bending energy of the filament. Figure 8(a) displays variation of bending energy of the filament with Pe. Bending energy increases linearly with Pe in the range of $l_a < 14$. For the $l_a > 14$, bending energy increases monotonically up to a certain Péclet number, after which an abrupt change in the bending energy appears specifically for $l_a = 14$, 20, and 25 as shown the Fig. 8(a). The transition point from the helical to the folded state is recognized from the sharp increase in the bending energy.

A sudden increase in the bending energy arises from the sharp buckling of the filament, which is uncorrelated over length scale larger than l_a. Therefore, a sharp buckled filament exhibits very high bending energy. Once again, it is important to mention here that elastic or bending energy does not show any sharp transition between the extended state to the helical or circular state. However, a folded state does show a sharp increase in the elastic energy. Furthermore, bending energies of the circular and the helical states exhibit similar behavior.

From the analysis of the torsional order parameter, the bending energy, and the tangent-tangent correlation, different structures of the filament in the parameter space of Pe and spacing between active forces are recognized. A phase diagram is displayed in Fig. 8(b) as a function of Pe and l_a. The color map shows the variation in bending energy per monomer in different phases, and, similarly, the colors of the symbols are also changed in the plot. In the graph, extended state and uncorrelated folded state are separated by the green shaded area which reflects the helical and circular states.

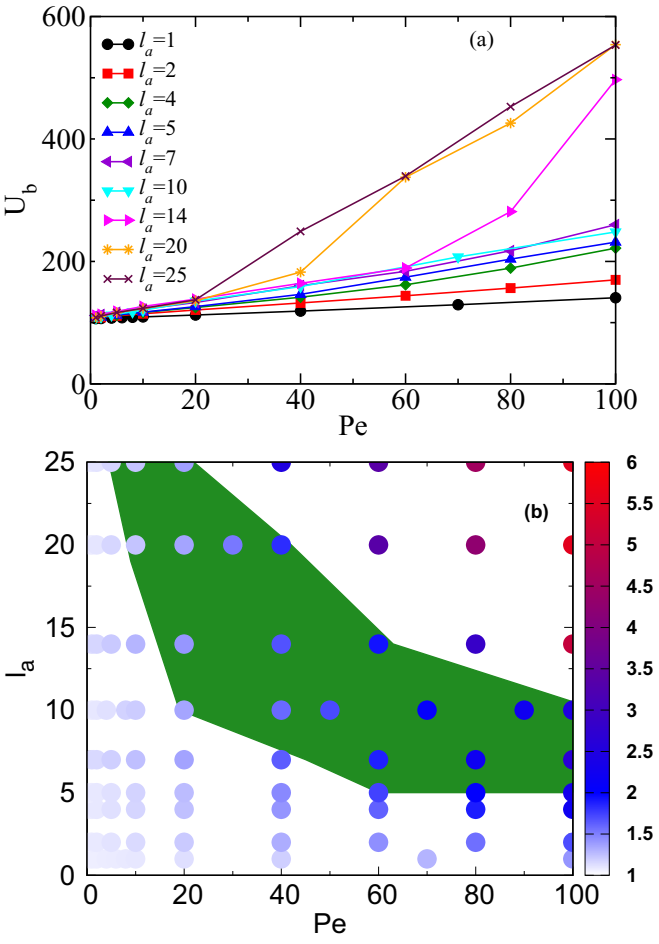

FIG. 8. (a) Average bending energy of the filament as a function of Pe for various spacing between active monomers. (b) Phase diagram for the equispaced activity on the polymer for a given $\kappa = 100$. The light blue circle on the graph shows extended structure, and the green shaded area represents the helical and circular structures. Above the green shaded area the folded state is represented. In order to accommodate equal spacing between the active monomers we have taken filament length $N = 99$ for the $l_a = 7$ and 14.

In the green shaded area, a circular phase appears for $l_a = 14$, 20, and 25 and a helical is for $l_a = 5$, 7, and 10. We are analyzing various structures in terms of bond correlation, torsional energy, and bending energy. These physical quantities do not show any significant change from circular to helical states as displayed in Figs. 6, 7, and 8(a). Thus in the phase diagram, a circular state is displayed together with the helical state. The region below the green shaded area represents the extended state, and above the shaded area corresponds to the folded state. Below the green area an extended phase appears, which exists in a smaller separation limit $l_a \leqslant 4$ for all Pe. In addition, for large separations, the extended state appears in the limit of small Péclet number.

V. SUMMARY AND CONCLUSIONS

In this article, we have performed a detailed study of the structural and dynamical behaviors of a freely moving self-propelled filament in three dimensions. The location and

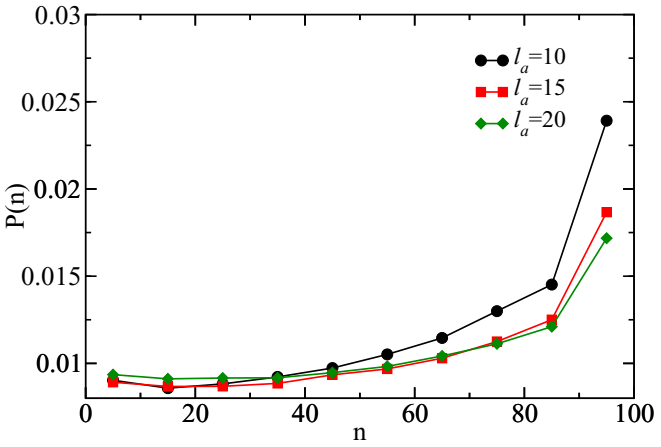

FIG. 9. The distribution of active sites on the filament for the rodlike structure. Here $n = 100$ corresponds to the head (front monomer) of the filament and $n = 1$ is the tail.

the number of self-propelled monomers are considered as a variable, and they are mimicked in two different ways: homogeneously, i.e., on all monomers, and periodic sequence of the self-propulsion on the filament.

In homogeneous self-propulsion, the radius of gyration and the end-to-end distance decrease with increasing active force for all bending parameters. We have shown that the change in structural properties for various rigidities can be described by flexure number with a single master curve in the limit of $\chi \leqslant 1$. Similarly, our analysis also reveals that the persistence length of the polymer decreases with active force, and a universal behavior for all bending parameters is also shown in the limit of $\chi \leqslant 1$. The translation motion is dominant for $\chi << 1$, and thus it assumes the extended state. In the limit of $\chi \approx 1$, the polymer gradually enters from semiflexible to flexible limit where it attains a coil-like structure. The latter state is more favorable in the presence of large fluctuations due to higher entropy.

The sequential arrangement of active monomers shows the large-scale conformational transition even at fewer number of active monomers and small force limit. In this case, a filament acquires extended, circular, helical, and folded structures. A helical or circular phase appears for larger separation of active monomers $l_a \geqslant 5$, and under strong compressive force Pe $>$ 1. For the larger separations, smaller active force is sufficient for the formation of helical structure. This state occurs due to the competition among drag, active, and bending forces. A larger load applies more drag on the active monomers that requires a larger force to push the filament. If active force is weaker to drag the passive monomers, then active energy is converted into buckling of the filament. The transition point is recognized from the tangent-tangent correlation, which shows crossover from exponential decay to oscillatory behavior [36]. A large torsional order parameter also confirms twisting and long-range ordering of bonds on the filament [12].

The load in a patterned case is very crucial at intermediate separations. Several interesting structures appear for large separations, i.e., $l_a \geqslant 5$. Here the polymer buckles under the load in front of an active monomer that translates to the entire polymer due to large separation among the active monomers. This leads to the rotation of the filament. Thus the presence of load and regular arrangement of the activity causes correlated buckling, which translates into circular, helical, or folded structures. On the other hand, if the first monomer is also considered as active for $l_a \geqslant 5$ (without load), then it pulls the filament from the front end, which suppresses buckling between the first two active monomers and causes translation of the filament.

Furthermore, to display the importance of the load on the active filaments, we perform simulations with randomly placed active monomers (termed here inhomogeneous self-propulsion). In this case, few monomers are randomly chosen to be active whose locations are also shuffled at new uncorrelated locations with time. The shuffling is done in the fixed time interval chosen in such a way that it is larger than the longest relaxation time of the filament. A filament acquires structures similar to the periodic arrangement, and these structures display a strong correlation with the location of the active monomers and their numbers.

We chose to analyze here only rodlike states under inhomogeneous self-propulsion. If $R_e \geqslant 0.9Nl_0$, then it is assumed to be in the rodlike state. We identify the probability distribution of active monomers for a rodlike structure under inhomogeneous self-propulsion. The distribution of active sites (Fig. 9) reflects that the probability of the front few monomers to be active is nearly 3 times higher relative to others. This can be interpreted as follows: The presence of a large number of active sites in the front drags the filament easily through the medium, and therefore it may always stay in the extended state. This is similar to pulling a filament by a constant force. Therefore, the presence of a load is very crucial for the transition from the extended to the helical, circular, and folded states.

A filament under inhomogeneous viscous drag often buckles in a helical or U-shaped structure [12,48]. Such structures are very common in biological systems, for example, the beating motion of sperm and *Caenorhabditis elegans*, and the helical structure of bacterial flagella [4–6]. In summary, we have identified that a freely swimming filament assumes the helical phase in the presence of load at the front end, which, to our knowledge, has not been investigated in any previous study. The curvature radius of the helical state shows a power-law behavior as $R_\beta \sim \mathrm{Pe}^{-\beta}$, $\beta \sim 0.55$. The strong buckling of the filament under the periodic arrangement of the active force may provide insight into the understanding of mechanical responses of actin filaments in the presence of molecular motors [49,50]. It would be interesting to explore the conformations of the filament under inhomogeneous self-propulsion in detail. This case may be able to provide a better comparison for experimental systems where the medium is more complex and heterogeneous.

ACKNOWLEDGMENTS

We thank DST SERB Grant No. YSS/2015/000230 for financial support. The authors acknowledge use of the high-performance computing facility at IISER Bhopal.

[1] T. Vicsek, A. Czirók, E. Ben-Jacob, I. Cohen, and O. Shochet, Phys. Rev. Lett. **75**, 1226 (1995).

[2] J. K. Parrish and W. M. Hamner, *Animal Groups in Three Dimensions: How Species Aggregate* (Cambridge University Press, Cambridge, 1997).

[3] C. Dombrowski, L. Cisneros, S. Chatkaew, R. E. Goldstein, and J. O. Kessler, Phys. Rev. Lett. **93**, 098103 (2004).

[4] M. C. Marchetti, J. F. Joanny, S. Ramaswamy, T. B. Liverpool, J. Prost, M. Rao, and R. A. Simha, Rev. Mod. Phys. **85**, 1143 (2013).

[5] J. Elgeti, R. G. Winkler, and G. Gompper, Rep. Prog. Phys. **78**, 056601 (2015).

[6] C. Bechinger, R. Di Leonardo, H. Löwen, C. Reichhardt, G. Volpe, and G. Volpe, Rev. Mod. Phys. **88**, 045006 (2016).

[7] A. Ghosh and N. Gov, Biophys. J. **107**, 1065 (2014).

[8] T. Eisenstecken, G. Gompper, and R. G. Winkler, Polymers **8**, 304 (2016).

[9] T. Eisenstecken, G. Gompper, and R. G. Winkler, J. Chem. Phys. **146**, 154903 (2017).

[10] H. Jiang and Z. Hou, Soft Matter **10**, 1012 (2014).

[11] A. Kaiser, S. Babel, B. ten Hagen, C. von Ferber, and H. Löwen, J. Chem. Phys. **142**, 124905 (2015).

[12] R. Chelakkot, R. G. Winkler, and G. Gompper, Phys. Rev. Lett. **109**, 178101 (2012).

[13] R. E. Isele-Holder, J. Elgeti, and G. Gompper, Soft Matter **11**, 7181 (2015).

[14] R. E. Isele-Holder, J. Jager, G. Saggiorato, J. Elgeti, and G. Gompper, Soft Matter **12**, 8495 (2016).

[15] A. Laskar and R. Adhikari, New J. Phys. **19**, 033021 (2017).

[16] D. Sarkar and S. Thakur, Phys. Rev. E **93**, 032508 (2016).

[17] J. Howard *et al.*, *Mechanics of Motor Proteins and the Cytoskeleton* (Sinauer Sunderland, MA, 2001).

[18] C. Brennen and H. Winet, Annu. Rev. Fluid Mech. **9**, 339 (1977).

[19] R. Lyons, E. Saridogan, and O. Djahanbakhch, Hum. Reprod. Update **12**, 363 (2006).

[20] O. C. Rodriguez, A. W. Schaefer, C. A. Mandato, P. Forscher, W. M. Bement, and C. M. Waterman-Storer, Nat. Cell Biol. **5**, 599 (2003).

[21] T. Vicsek and A. Zafeiris, Phys. Rep. **517**, 71 (2012).

[22] M. Abkenar, K. Marx, T. Auth, and G. Gompper, Phys. Rev. E **88**, 062314 (2013).

[23] S. J. DeCamp, G. S. Redner, A. Baskaran, M. F. Hagan, and Z. Dogic, Nat. Mater. **14**, 1110 (2015).

[24] Y. Sumino, K. H. Nagai, Y. Shitaka, D. Tanaka, K. Yoshikawa, H. Chaté, and K. Oiwa, Nature **483**, 448 (2012).

[25] V. Schaller, C. Weber, E. Frey, and A. R. Bausch, Soft Matter **7**, 3213 (2011).

[26] V. Schaller and A. R. Bausch, Proc. Natl. Acad. Sci. USA **110**, 4488 (2013).

[27] R. Chelakkot, A. Gopinath, L. Mahadevan, and M. F. Hagan, J. R. Soc., Interface **11**, 20130884 (2014).

[28] N. Samanta and R. Chakrabarti, J. Phys. A: Math. Theor. **49**, 195601 (2016).

[29] H. Vandebroek and C. Vanderzande, Phys. Rev. E **92**, 060601 (2015).

[30] D. Osmanovic and Y. Rabin, Soft Matter **13**, 963 (2017).

[31] S. Maharana, D. Sharma, X. Shi, and G. Shivashankar, Biophys. J. **103**, 851 (2012).

[32] S. Talwar, A. Kumar, M. Rao, G. I. Menon, and G. Shivashankar, Biophys. J. **104**, 553 (2013).

[33] S. C. Weber, A. J. Spakowitz, and J. A. Theriot, Proc. Natl. Acad. Sci. USA **109**, 7338 (2012).

[34] A. Zidovska, D. A. Weitz, and T. J. Mitchison, Proc. Natl. Acad. Sci. USA **110**, 15555 (2013).

[35] C. P. Brangwynne, G. H. Koenderink, F. C. MacKintosh, and D. A. Weitz, Phys. Rev. Lett. **100**, 118104 (2008).

[36] L. Giomi and L. Mahadevan, Phys. Rev. Lett. **104**, 238104 (2010).

[37] K. Sekimoto, N. Mori, K. Tawada, and Y. Y. Toyoshima, Phys. Rev. Lett. **75**, 172 (1995).

[38] R. G. Winkler, P. Reineker, and L. Harnau, J. Chem. Phys. **101**, 8119 (1994).

[39] L. Harnau, R. G. Winkler, and P. Reineker, J. Chem. Phys. **106**, 2469 (1997).

[40] O. Kratky and G. Porod, J. Colloid Sci. **4**, 35 (1949).

[41] N. Saitô, K. Takahashi, and Y. Yunoki, J. Phys. Soc. Jpn. **22**, 219 (1967).

[42] H.-P. Hsu, W. Paul, and K. Binder, Europhys. Lett. **92**, 28003 (2010).

[43] H.-P. Hsu, W. Paul, and K. Binder, Europhys. Lett. **95**, 68004 (2011).

[44] D. Loi, S. Mossa, and L. F. Cugliandolo, Soft Matter **7**, 10193 (2011).

[45] J. Palacci, C. Cottin-Bizonne, C. Ybert, and L. Bocquet, Phys. Rev. Lett. **105**, 088304 (2010).

[46] See Supplemental Material at http://link.aps.org/supplemental/10.1103/PhysRevE.98.042501 for three movies showing structures of the filament under a periodic sequence of the self-propulsion.

[47] J. P. Kemp and Z. Y. Chen, Phys. Rev. Lett. **81**, 3880 (1998).

[48] D. Steinhauser, S. Köster, and T. Pfohl, ACS Macro Lett. **1**, 541 (2012).

[49] T. Sanchez, D. T. Chen, S. J. DeCamp, M. Heymann, and Z. Dogic, Nature **491**, 431 (2012).

[50] T. Sanchez, D. Welch, D. Nicastro, and Z. Dogic, Science **333**, 456 (2011).